AIAA JOURNAL
Vol. 43, No. 5, May 2005

Eddy-Current-Based Momentum Transfer Method to Suppress Three-Dimensional Separation

Datta V. Gaitonde* and James H. Miller†
U.S. Air Force Research Laboratory, Wright–Patterson Air Force Base, Ohio 45433

A magnetogasdynamic technique is explored to alleviate separation in a three-dimensional crossing-shock turbulent boundary-layer interaction. An eddy-current-based momentum transfer mechanism is proposed to enhance the momentum of near-wall fluid by generating appropriate accelerating forces. An established numerical methodology, blending first-principles and phenomenological models, is utilized to demonstrate the technique to eliminate secondary separation observed in strong interactions. The circulating current is generated by applying a uniform magnetic field in an electrically conducting region spanning both near-wall low-momentum regions as well as high-speed outer flow and bounded by insulated walls. The "trapping" of electrical current is ensured by the generation of an induced electric field, which overwhelms the motional electromotive field near the surface. Under these conditions, ponderomotive forces slow the outer fluid while accelerating the near-wall low-speed regime, thus enhancing its ability to overcome adverse pressure gradients without separation. The complex and highly three-dimensional interplay between velocity, magnetic, current, and electric field vectors is described. Effects of force and heat release are differentiated through discriminating simulations. Despite complete local laminarization of the flow by the damping effect of the magnetic field, near-wall accelerating forces eliminate manifestations of secondary separation. In contrast, heating, by itself, aggravates secondary separation.

Nomenclature

A	=	amplitude of σ distribution
a	=	width of σ distribution
$\boldsymbol{B}$	=	magnetic induction
C_I^M	=	coefficient in k–ϵ magnetic field terms
C_p	=	specific heat at constant pressure
$\boldsymbol{E}$	=	electric field
e	=	total energy
F, G, H	=	flux vectors
J	=	metric Jacobian
$\boldsymbol{j}$	=	current
k	=	thermal conductivity coefficient; turbulence energy
L	=	length scale
M	=	Mach number
n	=	exponent in σ distribution
Pr	=	Prandtl number
Pr_t	=	turbulent Prandtl number
P_0	=	total pressure
p	=	pressure
Q	=	magnetic interaction parameter or Stuart number
Q_c	=	heat-release term
Q_{ht}	=	heat-conduction term
R	=	line of attachment
Re	=	Reynolds number
R_σ	=	magnetic Reynolds number
S	=	source vector; line of separation
s	=	distance variable in σ distribution
T_w	=	wall temperature
T_0	=	total temperature
t	=	time
$\boldsymbol{U}$	=	velocity
$\boldsymbol{X}$	=	flux vector of conserved quantities; nondimensionalized distance
x, y, z	=	Cartesian coordinates
γ	=	ratio of specific heats
δ	=	boundary-layer thickness
ϵ	=	dissipation of turbulence energy
κ	=	coefficient in MUSCL reconstruction
μ	=	molecular viscosity
μ_t	=	eddy viscosity
ξ, η, ζ	=	curvilinear coordinates
ρ	=	density
σ	=	electrical conductivity
$\tilde{\tilde{\sigma}}$	=	electrical conductivity tensor
$\bar{\bar{\tau}}$	=	shear-stress tensor
ϕ	=	electric potential

Subscripts

I	=	inviscid
ref	=	reference values
V	=	viscous

Received 9 April 2004; revision received 15 November 2004; accepted for publication 11 December 2004.

*Technical Area Leader, Computational Sciences Branch, Aeronautical Sciences Division, Air Vehicles Directorate. Associate Fellow AIAA.

†Research Aerospace Engineer, Computational Sciences Branch, Aeronautical Sciences Division, Air Vehicles Directorate. Associate Fellow AIAA.

I. Introduction

PLASMA-BASED techniques exploiting electromagnetic forces for flow control are currently of considerable interest, both for high-speed as well as low-speed applications. The absence of moving parts is a particularly attractive feature of such methods in high-speed flows, where moving appendages can exhibit significant loss of effectiveness and exacerbate thermomechanical loads. Although the potential of electromagnetic interactions to alleviate or eliminate many of the pressing obstacles to accomplishing hypersonic flight has been known for some time, and many theoretical, experimental and numerical efforts[1–3] have been published, details of plasma interaction with the fluid dynamics remain largely unknown.

Numerical exploration of new flow management concepts has become increasingly feasible through the development of advanced numerical techniques,[4,5] and a select survey of applications has been presented in Ref. 6. In a previous set of publications,[7,8] we describe the systematic development of a robust and efficient tool based on the Navier–Stokes equations, supplemented with models of varying levels of sophistication for electromagnetic interaction, to obtain

insight into fluid response to plasma perturbations. To restrict computational effort at a reasonable level, a blend of phenomenological and first principles approaches has been adopted. Particular emphasis is placed on fully three-dimensional flows because two-dimensional and inviscid analyses cannot reproduce the complicated physics, which depend on the relative spatial orientation of the velocity, magnetic, electric, and current fields. The methodology on which the present effort is based has been verified and validated extensively[9–11] and is described briefly in Sec. II.

In this paper, an exploratory study is presented of the use of magnetogasdynamic (MGD) forces to suppress separation. Several issues pertinent to the use of MGD to control separation have been discussed in Ref. 12, together with experimental data. In contrast to the global goals of approaches such as the energy bypass method described in Ref. 13 and examined numerically in Ref. 7, the problem considered emphasizes local flow control. In the absence of an electric field, magnetic forces are typically retarding in nature and tend to induce separation through a mechanism similar to that established by adverse pressure gradients.[14] Local accelerating forces can be generated by appropriately oriented applied or induced electric fields in addition to magnetic fields. For steady situations, applied electric fields typically require electrodes, which can yield considerable local Joule heating, and have the potential to aggravate already high heat loads encountered in high-speed flight.[15]

Here we consider induced electric fields arising from a properly configured electrode-less electromagnetic interaction to accelerate near-wall fluid. As a prototypical fully three-dimensional situation, the turbulent flow past a double-fin configuration is considered, as shown schematically in Fig. 1. The simulation mimics the experiments of Zheltovodov and Maksimov[16] and Schuelein and Zheltovodov[17] in which the freestream Mach number and stagnation conditions are $M = 4.961$, $P_0 = 2.2$ MPa, and $T_0 = 427$ K, resulting in a freestream unit Reynolds number of 36.5×10^6 per meter; an appropriate length scale is the nominal boundary-layer height at the fin leading edge, $\delta = 3.8$ mm, while the wall temperature is $T_w = 295$ K. The flow past this three-dimensional geometry has been examined numerically in several prior publications (e.g., see Refs. 18–20 and citations therein). The problem isolates the physics of instances where an incoming equilibrium turbulent boundary layer, such as that developing say on a fuselage, interacts with shock waves generated by two compression surfaces, which can be considered to represent sidewalls of an inlet. As the angles of the fins are increased, the interaction between the resulting shock waves and the boundary layer on the plate becomes stronger, and the flowfield exhibits multiple separation and attachment phenomena. A topological description of this evolution has been presented in Ref. 20. The primary focus is on the situation where the two fins are placed at 23×23 deg angles of attack to the incoming flow: this is among the strongest interactions explored to date. Previously verified and validated efforts have shown that under the conditions observed experimentally by Zheltovodov and Maksimov[16] and Schuelein and Zheltovodov[17] both simulation[20,21] and experiment show the occurrence of secondary separation (SS), which is elucidated in a later section and is the focus of the present flow control study. To provide reference lower strength interactions, where SS is absent, select results from an 18×18 interaction are also presented.

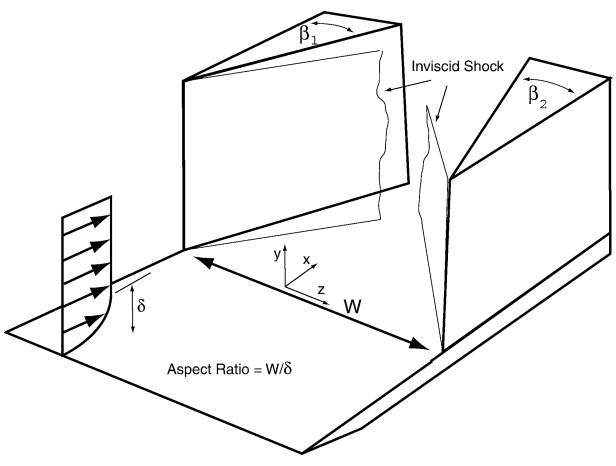

Fig. 1 Double-fin configuration.

The energy required for momentum enhancement is primarily obtained from the outer higher-speed, essentially inviscid flow. The key requirements are that the fluid be ionized through a suitable nonequilibrium ionization method and encompassing both high-speed and low-speed regions, that an appropriately oriented magnetic field be imposed, and that the walls be insulated. Under these conditions, an eddy (or circulating) current is generated in the flow. In the outer regions, the induced electric field is relatively weaker than the effective motional field, whereas the reverse situation holds near the surface. An analysis of the work performed on the fluid by the magnetic field, as accomplished in a subsequent section, shows that the momentum of the outer fluid is reduced, whereas that of the near-wall fluid is enhanced. This electrode-less approach, which effectively conveys momentum from high-speed to low-speed regions is thus designated the eddy-current-based momentum-transfer (ECBMT) method. The momentum transfer strengthens the boundary layer, which can then negotiate adverse pressure gradients without separation.

The paper is organized as follows. After a description of the theoretical model, Sec. II, the numerical scheme is outlined in Sec. III, which also cites various relevant code verification studies. In Sec. IV, previous non-MGD results reproduced for this effort are summarized with emphasis on validation and genesis of secondary separation. Subsequently, the effect of several control configurations including different MGD setups as well as volumetric heat release are also considered to clarify the principal mechanisms by isolating force and volumetric heating effects. The paper concludes after drawing several conclusions in Sec. V.

II. Governing Equations

The low-magnetic-Reynolds-number approximation ($R_\sigma = \mu_m \sigma U L \ll 1$) is invoked based on the anticipated environment for MGD control in aerospace applications. This permits the Navier–Stokes equations to be coupled to the ponderomotive force and electromagnetic energy through source terms:

$$\frac{\partial \rho^*}{\partial t^*} + \nabla^* \cdot (\rho^* \boldsymbol{U}^*) = 0 \tag{1}$$

$$\frac{\partial \rho^* \boldsymbol{U}^*}{\partial t^*} + \nabla^* \cdot [\rho^* \boldsymbol{U}^* \bar{\boldsymbol{U}}^* + p^* \bar{\bar{I}}] - \frac{1}{Re} \nabla^* \cdot \bar{\bar{\tau}}^* = Q(\boldsymbol{j}^* \times \boldsymbol{B}^*) \tag{2}$$

$$\frac{\partial \rho^* e^*}{\partial t^*} + \nabla^* \cdot \left[(\rho^* e + p^*) \boldsymbol{U}^* - \frac{1}{Re} (\boldsymbol{U}^* \cdot \bar{\bar{\tau}}^*) - \frac{1}{(\gamma - 1) Pr M^2 Re} Q^*_{\text{ht}} \right] = Q(\boldsymbol{E}^* \cdot \boldsymbol{j}^*) + Q_c \tag{3}$$

The superscript $*$ denotes a nondimensional quantity, $\boldsymbol{U} = \{u, v, w\}$ is the velocity vector, and $e = p/(\gamma - 1)\rho + \boldsymbol{U}^2/2$ is the total energy. Q_c is the heat-release term, which is employed only in one calculation designed to separate heating and work effects. The transport properties are the molecular viscosity μ, obtained with Sutherland's law, and the electrical conductivity σ, which, in this effort, is specified to match the profile anticipated from a suitable nonequilibrium ionization method. In addition to the Reynolds number $Re = \rho_{\text{ref}} U_{\text{ref}} L_{\text{ref}} / \mu_{\text{ref}}$, Mach number M, and Prandtl number $Pr = \mu_{\text{ref}} C_p / k_{\text{ref}}$, the interaction parameter $Q = \sigma_{\text{ref}} B^2_{\text{ref}} L_{\text{ref}} / (\rho_{\text{ref}} U_{\text{ref}})$ appears on the right-hand side. In the subsequent discussion, the superscript * will be suppressed, and all quantities will be assumed to be nondimensional unless explicitly otherwise stated. Algebraic manipulation permits the governing equations to be written in flux vector form:

$$\frac{\partial \hat{X}}{\partial t} + \frac{\partial \hat{F}_I}{\partial \xi} + \frac{\partial \hat{G}_I}{\partial \eta} + \frac{\partial \hat{H}_I}{\partial \zeta} = \frac{\partial \hat{F}_V}{\partial \xi} + \frac{\partial \hat{G}_V}{\partial \eta} + \frac{\partial \hat{H}_V}{\partial \zeta} + \hat{S} \tag{4}$$

where a general curvilinear coordinate transformation has been introduced, $x = x(\xi, \eta, \zeta)$, $y = y(\xi, \eta, \zeta)$, and $z = z(\xi, \eta, \zeta)$, in order

to facilitate the treatment of complex configurations. The solution vector X is $1/J\{\rho, \rho u, \rho v, \rho w, \rho e\}$, where J is the Jacobian of the coordinate transformation. F_I, G_I, and H_I contain terms relevant to inviscid fluxes while F_V, G_V, and H_V include effects caused by viscosity, and S is the source term describing the effects of electromagnetic interaction with the flow. The various vectors of Eq. (4) have been detailed in Refs. 9 and 10.

The current vector $\boldsymbol{j}$ is obtained from the phenomenological form of the generalized Ohm's law[22]:

$$\boldsymbol{j} = \tilde{\tilde{\sigma}} \cdot [\boldsymbol{E} + \boldsymbol{U} \times \boldsymbol{B}] \tag{5}$$

The term arising from electron pressure gradients has been neglected because it is anticipated to be small.[23] In the general case, the tensor conductivity $\tilde{\tilde{\sigma}}$ includes the Hall and ion-slip parameters. Although the anticipated environment can be susceptible to effects associated with the Hall current, which serves generally to diminish the strength of the current, in the present case the effect is expected to be higher order because of the imposition of insulated walls and relatively low concomitant current magnitudes. Detailed expressions for the source terms as well as the conductivity have been provided in Ref. 24 and are not repeated here.

A key element of the proposed mechanism is the induced electric field which ensures that current flows in closed paths inside the fluid for compatibility with the electrically insulated wall-bounded condition of the region. The electric field $\boldsymbol{E}$ is determined from the current continuity condition:

$$\nabla \cdot \boldsymbol{j} = 0 \tag{6}$$

which yields a Poisson equation when a scalar potential, $\boldsymbol{E} = -\nabla\phi$ is introduced:

$$\nabla \cdot [\tilde{\tilde{\sigma}} \cdot [\nabla\phi]] = \nabla \cdot [\tilde{\tilde{\sigma}}(\boldsymbol{U} \times \boldsymbol{B})] \tag{7}$$

Insertion of an artificial time derivative term permits this equation also to be written in the scalar equivalent of Eq. (4)

$$\frac{\partial}{\partial\tau}\left(\frac{\phi}{J}\right) + \frac{\partial\hat{F}}{\partial\xi} + \frac{\partial\hat{G}}{\partial\eta} + \frac{\partial\hat{H}}{\partial\zeta} = 0 \tag{8}$$

This greatly facilitates the development of a unified solution procedure as described in Ref. 8 and outlined in Sec. III.

Although the magnetic field affects turbulence in a highly complex manner, an engineering approach is employed to mimic the effects of fine-scale turbulence. The method utilizes the popular two-equation k–ϵ model, where k is the turbulence kinetic energy and ϵ is its dissipation. New terms are added to the original model to reproduce some of the anticipated effects of the magnetic field in a simple yet effective manner based on the recent effort of Kenjeres and Hanjalic.[25] Thus, the mean flow equations are assumed to be of the same form as discussed earlier, with the molecular viscosity μ being replaced by the sum $\mu + \mu_t$, where μ_t is the eddy viscosity and a turbulent Prandtl number ($Pr_t = 0.9$) is introduced in the standard fashion. The baseline two-equation k–ϵ model, including low-Reynolds-number terms, employs the work of several authors and has been described in much greater detail in Ref. 24. Briefly, in flux vector form and curvilinear coordinates, the governing equations are

$$\frac{\partial X_{k\epsilon}}{\partial t} + \frac{\partial F_{k\epsilon}}{\partial\xi} + \frac{\partial G_{k\epsilon}}{\partial\eta} + \frac{\partial H_{k\epsilon}}{\partial\zeta} = S_{k\epsilon} \tag{9}$$

where

$$X_{k\epsilon} = \frac{1}{J}\begin{bmatrix}\rho k \\ \rho\epsilon\end{bmatrix} \tag{10}$$

Details of $F_{k\epsilon}$, $G_{k\epsilon}$, $H_{k\epsilon}$, and $S_{k\epsilon}$ have been presented in Ref. 24. The primary effect of the magnetic field appears in $S_{k\epsilon}$. Denoting the vector formed by these terms, representing the effect of the magnetic field on fine-scale turbulence as $S_{\mathrm{MHD},k\epsilon}$,

$$S_{\mathrm{MHD},k\epsilon} = -\frac{1}{J}\begin{bmatrix} Q\sigma\boldsymbol{B}^2 k e^{-C_1^M Q\sigma/\rho B^2(k/\epsilon)} \\ Q\sigma\boldsymbol{B}^2\epsilon e^{-C_1^M Q\sigma/\rho B^2(k/\epsilon)}\end{bmatrix} \tag{11}$$

The new coefficient introduced C_1^M is taken to be 0.025 as in Ref. 25.

III. Numerical Considerations

Because the influence of the magnetic field is restricted to the source term in the present low-R_σ approach, conventional computational-fluid-dynamics techniques are applied to the inviscid and viscous fluxes. Thus, for the inviscid fluxes the Roe[26] scheme is utilized with the nominally third-order $\kappa = \frac{1}{3}$ monotone upstream-centered scheme for conservation laws (MUSCL) reconstruction technique,[27] and the harmonic limiter described in Ref. 28 is employed to enforce monotonicity. Viscous terms are computed with standard central second-order differences. The turbulence transport equations are discretized in a similar fashion, that is, a MUSCL-based upwind approach is employed for the inviscid fluxes, and a second-order method is utilized for all diffusion and source terms.

The electromagnetic force terms require three quantities: the magnetic field, the electric current and the electric field. The first of these, $\boldsymbol{B}$ is specified to be uniform. The second $\boldsymbol{j}$ is obtained from the generalized Ohm's law with an assumed plasma conductivity environment described after the no-control flowfield is elucidated in Sec. IV. As noted earlier, the final component, the electric field, is obtained from a Poisson equation arising from the current continuity constraint. The spatial discretization for the electric potential is accomplished with fourth-order compact differences as described in Ref. 8. Because the flowfield contains shocks, differencing the source term in Eq. (7) to higher-order can introduce numerical instabilities. In such cases, smoothness is enforced with a Pade-type filter.[8]

All sets of equations for the fluid and turbulence quantities and the electric potential are integrated in time with the approximately factored Beam–Warming-type method as described in Ref. 24. By employing subiterations, tight coupling of the physical phenomena is ensured at the outer iteration level while the numerical advantages of fine-grain loose coupling are exploited at the inner iteration.

The configuration considered is symmetric. Consequently only half the domain is simulated. The grid employed is composed of sequential nonuniform Cartesian planes oriented normal to the freestream direction, with mesh points clustered to resolve high gradients near walls and in the interior. Meshes with 340 K, 2.6 M, and 5.3 M points are utilized to provide information on solution dependence. On all solid surfaces, the no-slip condition is enforced, the pressure gradient is assumed to be zero, and the case-dependent wall temperature is specified. Values of k and ϵ are also zero on solid walls because of the chosen formulation. For all cases considered, the downstream boundaries are predominantly supersonic. Consequently, the zero-gradient condition is applied. The inflow profile is determined from separate two-dimensional calculations so that the momentum thickness of the incoming equilibrium boundary layer matches that reported in the experiment of Ref. 16 ($\theta = 0.157$ mm). The boundary conditions on electrical variables are straightforward: because all walls are assumed to be insulators—this is a key requirement for the ECBMT method—the condition $\boldsymbol{j} \cdot \hat{n} = 0$ is enforced in the manner described in Ref. 8.

The methodology just described has been verified in many simulations, details of which are not repeated for the purposes of brevity. Two examples that have been previously published in the archival literature might however be noted because they demonstrate the ability to capture the effects of magnetic fields on shocks and smoother features such as boundary layers. In Ref. 11, numerical solutions for the flow past a blunt body were compared favorably to theoretical results of Ref. 29. Reference 14 contains several additional studies, including particularly a successful comparison with the theory of Ref. 30 on the effect of a variable magnetic field on the flow

past a flat-plate boundary layer. Validation of the three-dimensional double-fin computations (without MGD) are displayed next.

IV. Control of Separation in Swept Interactions

As noted earlier, the phenomenon of secondary separation occurring in the double-fin configuration of Fig. 1 is considered as a prototypical problem on which to apply the proposed control technique. Although the domain on only one side of the plane of symmetry is computed, for clarity some results are reflected prior to plotting. To set the stage for flow control, the baseline flow without MGD is first described briefly, following the development of Ref. 20.

Figure 2 depicts experimentally inferred and computed "surface streamlines." Various lines of coalescence S and divergence R have been marked. For consistency, the notation follows that employed by the experimentalists.[16] The primary lines (S_1, R_1), and their mirror image segments (S_2, R_2), represent primary separation and attachment. Downstream, the two primary lines of separation evolve into a complex structure yielding a centerline of attachment (R_3), which is not evident in the experiment but whose existence is required for consistency. R_3 is straddled by two lines of off-centerline separation (S_3', S_3'', and their mirror images). The line of coalescence, marked S_3, aligned along an angle approximately midway between the primary separation and attachment lines, marks SS, which is the major focus of the present attempt at MGD control. There is also a clearly identifiable attachment line R_3' in its close vicinity as required for consistency. The mirror images of these two lines

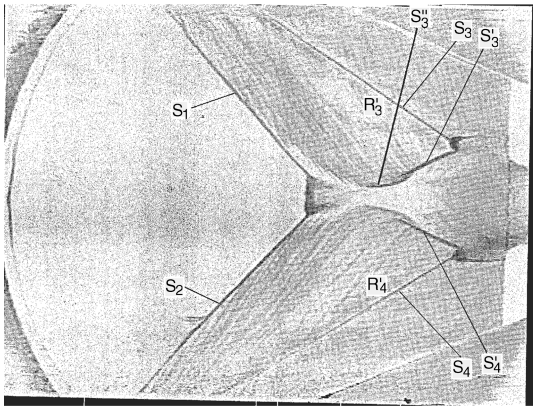

a) Experiment[16]

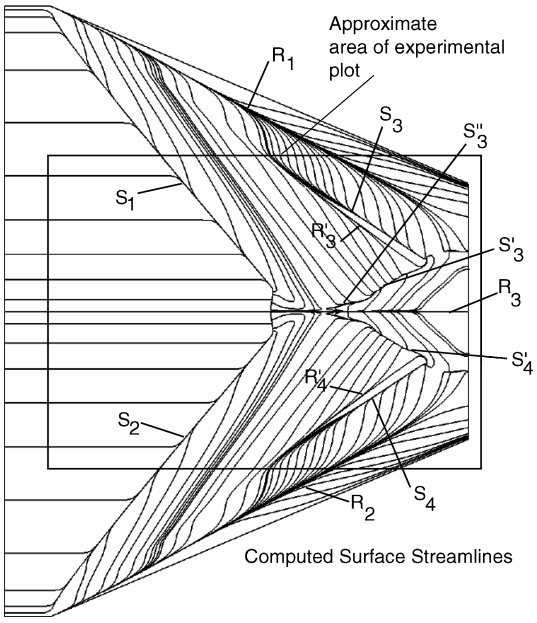

b) Computation

Fig. 2 Surface streamline structure in the 23 × 23 deg interaction.

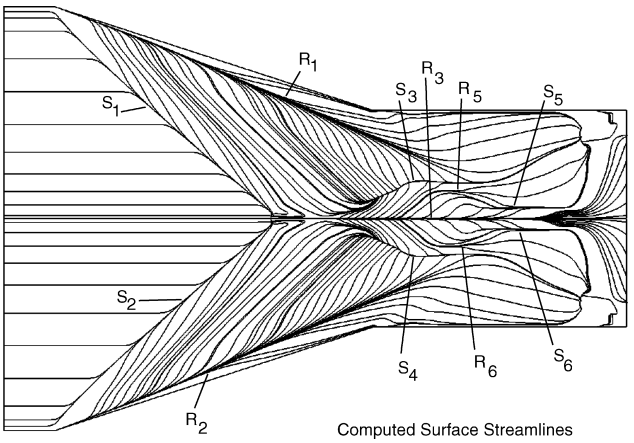

Fig. 3 Surface streamline structure in the 18 × 18 deg interaction.

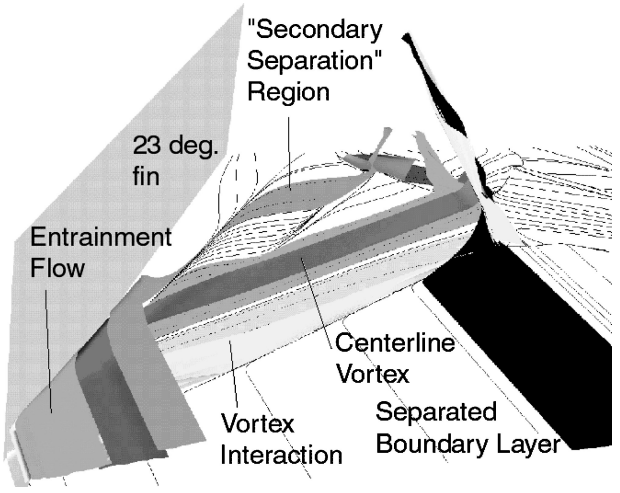

Fig. 4 Double-fin flowfields for strong interaction strength.

are denoted S_4 and R_4'. These lines terminate downstream where they form a critical point pair (not marked) with S_3'. Although SS is commonly observed in laminar flows, the phenomenon is relatively rare in shock/turbulent boundary-layer interactions. It has however been previously reported in experiments and computations on strong single-fin-on-plate interactions.[31–33] Available evidence suggests that the phenomenon occurs only in a narrow range of interaction parameters.[34] Indeed, the surface oil flow pattern for the 18×18 interaction, introduced in Fig. 3 as a reference, does not show SS (the comparison with experiment for this case is similarly excellent; see Ref. 20). However, other features observed in Fig. 2, including primary and centerline lines of attachment and separation, are clearly evident in Fig. 3 as well.

The three-dimensional flowfield for the 23×23 interaction is exhibited in Fig. 4 in terms of ribbons formed by joining judiciously chosen particle traces to provide insight into coherent structures that comprise the flowfield. The incoming boundary layer separates along the primary separation line and does not reattach but, rather, becomes narrow and curved downstream (only a part of this surface is shown to visualize the other regimes). Fluid attaching at the primary line of attachment R_1 can be distinguished into three different components. The vortex interaction regime contains the fluid that separates from the downstream side of S_1. A vortex filament pair (not shown) originates from two foci on either side of the symmetry plane. The second regime consists of fluid separating at S_3'', whereas the last regime comprises flow attaching at R_1 and separating at the line of SS, S_3. Fluid attaching at the centerline R_3 originates outside the incoming boundary layer from near the fin leading edges and sweeps across the domain prior to attachment. The region between R_3 and S_3', S_3'' is the footprint of one of the symmetric pair of centerline vortices.

A detailed discussion of the dynamics of SS has been presented in Ref. 20. Fluid attaching at the primary attachment lines is essentially downstream of the inviscid shock front. The subsequent spanwise motion is initially accompanied by a generally favorable pressure gradient. Pressure contours at several spanwise locations are shown in Fig. 5a. To provide a reference, the surface oil flow pattern is also plotted, and select lines of coalescence and divergence are identified. For subsequent discussion, quantities on the plane corresponding to $X = 40.5$ will be examined in greater detail. Pressure and velocity-magnitude contours (on only one side of the plane of symmetry) are shown in Figs. 5b and 5c. Far from the plate, the intersection of the inviscid shock caused by the fin with the cross-flow plane is clearly observed. The interaction of the shock with the boundary layer produces the classic three-dimensional λ pattern whose features have been described extensively elsewhere.[35] The two λ from either side of the symmetry plane cross each other in downstream regions, in a complex manner that has been described in Ref. 36. Velocity magnitude contours show the entrainment of high-speed fluid near the plate. The ECBMT method to be employed requires that the ionized region extend into high-velocity regions, to establish the required electromotive forces (emf). Consequently, entrainment greatly reduces the required height of the conducting region.

Figure 6a depicts surface pressure vs spanwise coordinate, at $X = 40.5$ on several meshes, together with experimental data. Figure 6b shows similar results for the weaker 18×18 interaction as a reference case in which secondary separation does not occur. The solution can be considered to be grid independent, with modest sensitivity being restricted to the region near attachment, $Z \sim -19$. The sharp reduction in pressure between attachment and $Z \sim -14$ is associated with the expansion of the attaching postshock fluid as it moves in the generally spanwise direction. The subsequent pressure rise at $Z \sim -13$ is correlated to the observed SS point, although it is emphasized that an analysis based on spanwise pressure gradient is a simplified view because near-wall fluid also has a sizeable streamwise component of velocity. Comparison of surface pressure with experiment in Fig. 6 is observed to be generally excellent, except at the symmetry plane, where significant overprediction is observed. A possible explanation for this discrepancy is described in the next

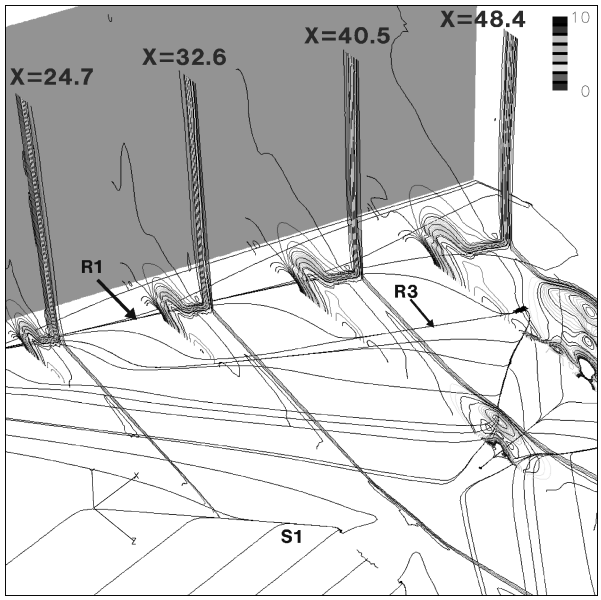

a) Perspective view of pressure on several planes

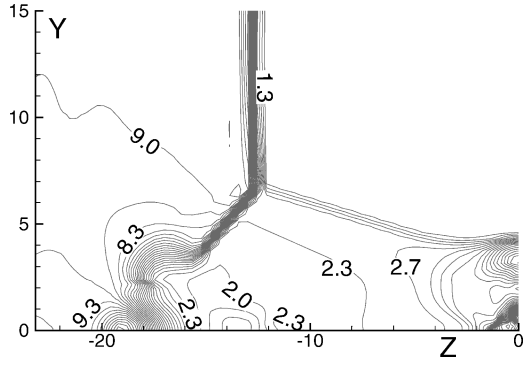

b) Pressure on cross-flow plane, $X = 40.5$

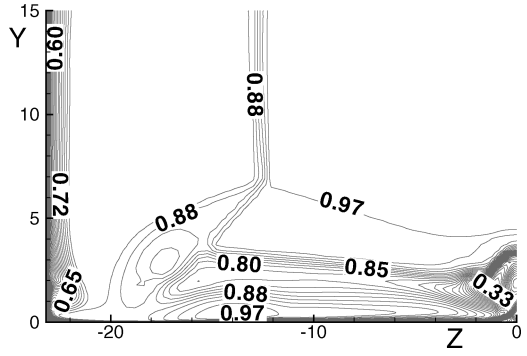

c) Velocity magnitude on cross-flow plane, $X = 40.5$

Fig. 5 Aspects of baseline (no-MGD) flow.

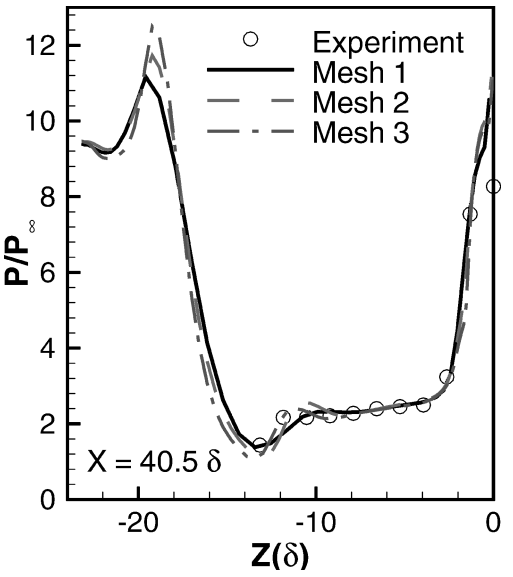

a) 23×23, $X = 40.3$

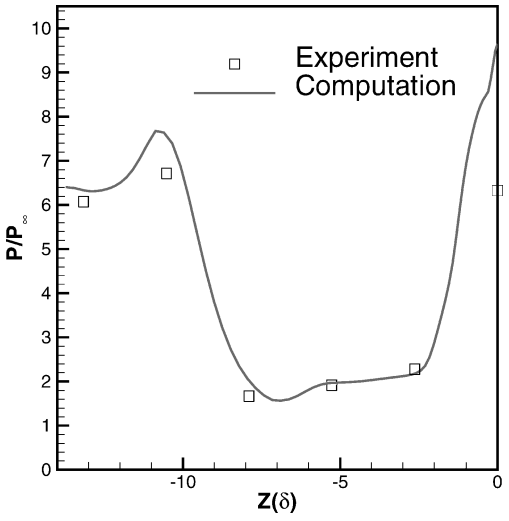

b) 18×18, $X = 37$

Fig. 6 Surface pressure along spanwise cuts.

paragraph. In the weaker 18×18 interaction, depicted in Fig. 6b, pressure levels are lower, but the comparison with experiment is again generally excellent except near the symmetry plane. A small local increase in pressure is perceptible at $Z \sim -7$ but, as noted earlier, is not accompanied by SS.

The effect of the initial favorable pressure gradient after primary attachment is to reduce the eddy viscosity near the plate, as shown in Fig. 7, which depicts contours on the $X = 40.5$ crossflow plane. The turbulence model successfully reproduces this anticipated relaminarization trend without any additional modifications. Values of eddy viscosity are the highest, reaching up to 1500 times the molecular viscosity, near the centerline, where the largest discrepancies were observed in surface-pressure predictions. This region is dominated by the complex three-dimensional centerline vortex pair (Fig. 4), where the turbulence model developed mainly from two-dimensional, mean steady considerations fails locally. The constrained region of the centerline vortices minimizes errors associated with the turbulence model from spreading outside of this region through convection or diffusion.

The objective of the MGD-control method explored is to increase the momentum of the near-wall fluid so that the adverse pressure gradient is either eliminated or can be successfully negotiated by the near-wall flow without SS. As noted earlier, the approach seeks to accomplish transfer of momentum from the high-speed outer region of the interaction to the near-wall fluid. Figure 8 shows schematically the configuration required to accomplish ECBMT in the double-fin

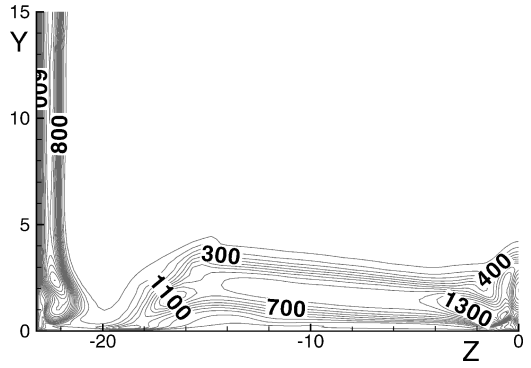

Fig. 7 Eddy viscosity μ_t/μ_{ref} on crossflow plane, $X = 40.5$.

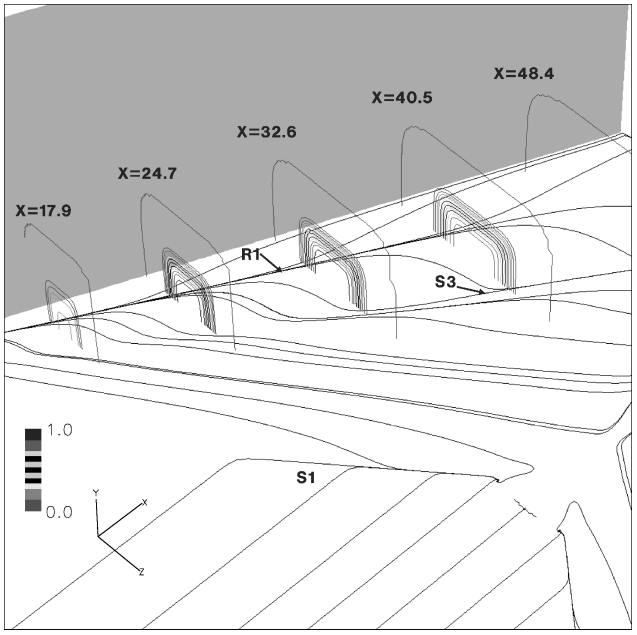

a) Perspective view with no-MGD surface streamlines

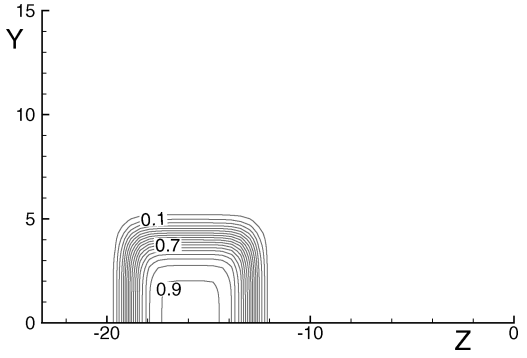

b) Cross-flow plane, $X = 40.5$

Fig. 9 Electrical conductivity σ distribution.

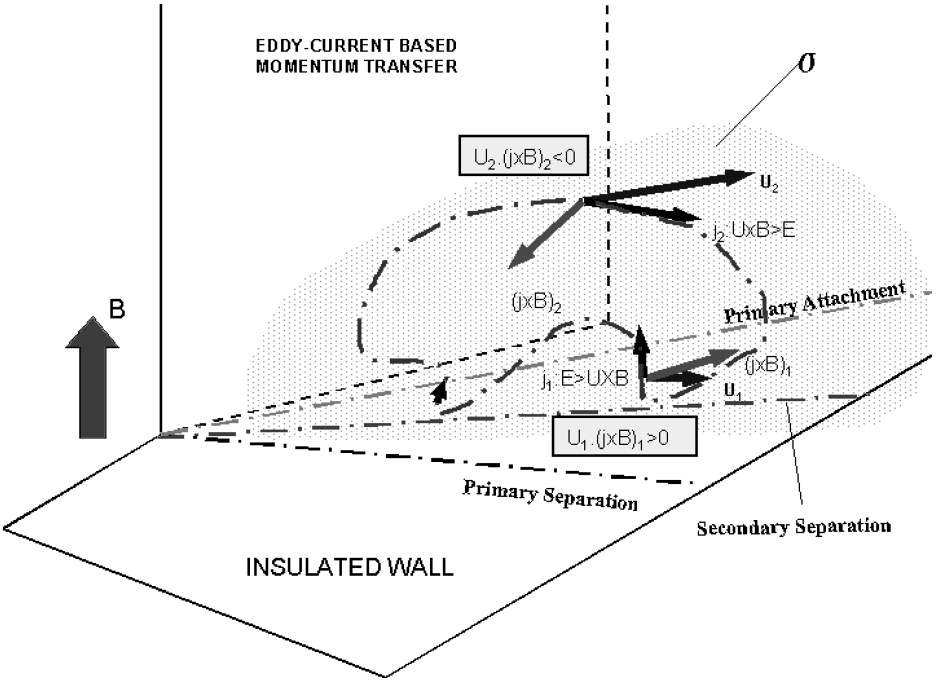

Fig. 8 Schematic of ECBMT method.

interaction. The region between R_1 and S_3 is assumed to be the footprint of a domain of ionization, extending a few boundary-layer heights above the plate. A uniform transverse magnetic field is established through an external agency, and both walls are assumed to be insulated. A complex fluid-plasma interaction arises, depending on the interplay between the velocity, magnetic, current, induced electric, and ponderomotive force fields. In regions of high velocity, the motional emf ($\boldsymbol{U} \times \boldsymbol{B}$) dominates the induced electric field. Here the local interaction is generator-like: Lorentz forces reduce fluid speed, and work is done in establishing the current [$\boldsymbol{U} \cdot (\boldsymbol{J} \times \boldsymbol{B}) < 0$]. Because eddy currents must be established, the reverse dynamic occurs in the near-wall low-speed region, where fluid is accelerated, that is, $\boldsymbol{U} \cdot (\boldsymbol{J} \times \boldsymbol{B}) > 0$. Appropriate establishment of the plasma environment thus has the potential to effectively transfer momentum from high-speed regions to low-speed regions to eliminate or reduce separation.

The ECBMT approach to alleviating separation is explored through several simulations. In each case, the electrical conductivity is established through a product of x, y, and z direction modified Gaussian's (MG), whose general form is

$$\sigma_1(A, a, s, s_0, n) = Ae^{-a(s-s_0)^n} \tag{12}$$

Here A is the peak (set to unity for normalized values); a determines the width; s is the distance variable, centered at s_0; and n is the exponent, which is set to 6. The constant a is determined by specifying a value of conductivity, ϵ at a specified distance δ from the center s_0 through $a = (1/\delta^n)\log(A/\epsilon)$. The approach loosely mimics the anticipated nonequilibrium ionization environment described in Ref. 1.

Perspective views of the conducting region are shown in Fig. 9a, and the profile in a crossflow plane is shown in Fig. 9b. In the streamwise direction, the electrically conducting region extends from the location, where S_3 is first detected to the point where it terminates. The spanwise MG extends from R_1 to S_3. Ionized regions of two different heights are explored, the first, H5, extending 5δ and the second, H2, extending only 2δ. For the first region, the interaction parameter is set to 1 (case H5Q1), whereas several interaction parameters are explored for the second, including 0.1 (H2Q0.1), 1 (H2Q1), and 5 (H2Q5). At $Q = 1$, reference values pertinent to the local low-velocity, low-density region where control is applied yield $\sigma B^2 \sim 200$ mho $\cdot$ T/m. These magnitudes are consistent with system studies[1,2] and depend on the freestream parameters, which here are chosen to match experiments for validation purposes (without magnetohydrodynamics). Operation in a high-altitude lower density environment will reduce the required plasma perturbation. For comparison purposes, a separate computation also considers simple heat release, distributed spatially in a manner similar to the electrical conductivity. However, the height is restricted to 0.5, and the normalized heat-release parameter $Q_c^* = Q_c L_{\text{ref}}/(\rho_{\text{ref}} U_{\text{ref}}^3)$ is set to 0.2, as a representative value based on the observed features of the Joule heating when MGD control is on.

Figure 10 shows the simulated surface oil flow pattern for several cases. The no-MGD solution has been replotted for ready reference in Fig. 10a. Close scrutiny of these figures (see inset of each) reveals that the effect of MGD is to eliminate or at least diminish the clarity of the secondary separation and attachment lines. For H2Q1, streamlines continue to converge in the region where SS exists in the no-MGD case, but do not form a distinct line of coalescence. The taller ionized domain, H5Q1, is more effective in that lines are more conical in form, with an increased streamwise component compared to the no-MGD case, and no traces of the original SS and attachment lines are evident. In both MGD cases, off-centerline separation S_3'' is not interrupted by critical points. Results obtained with $Q = 0.1$, not shown, indicate that this smaller interaction parameter is insufficient to create the desired effect. Heat release alone, that is,

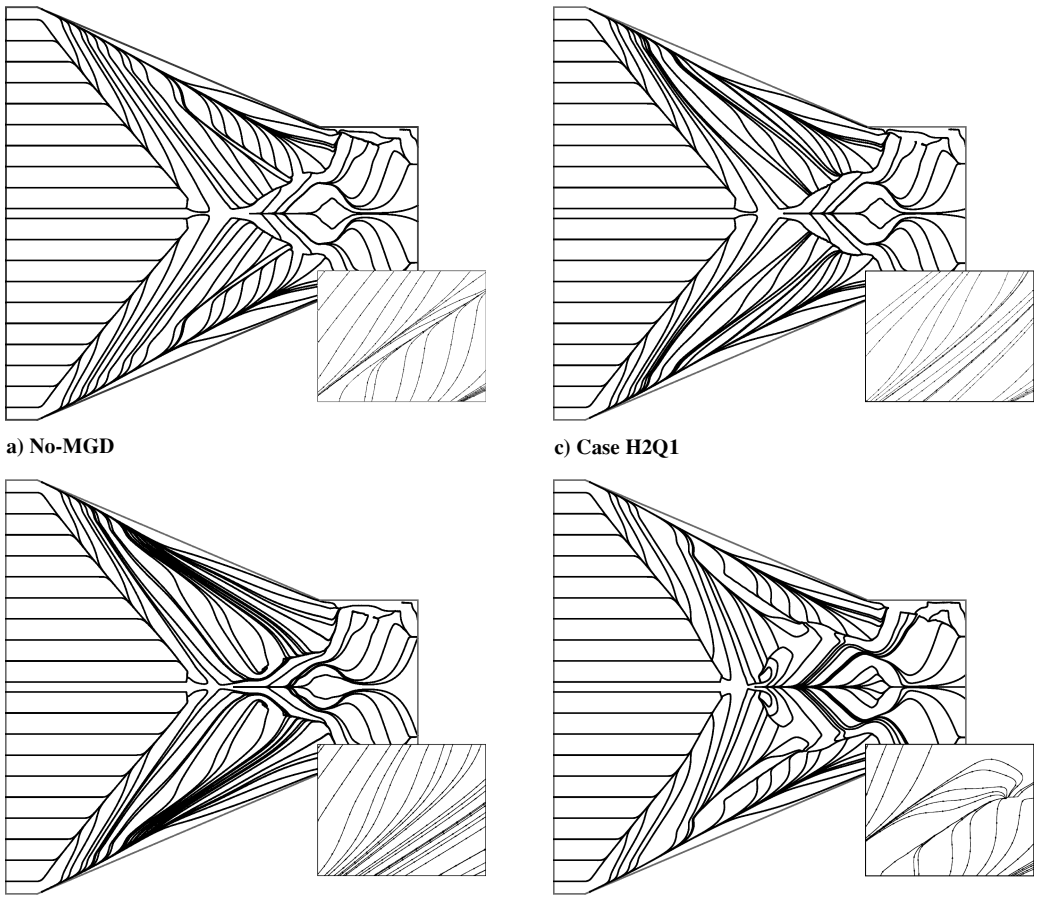

a) No-MGD **c) Case H2Q1**

b) Case H5Q1 **d) Case HR**

Fig. 10 Simulated surface oil flow lines.

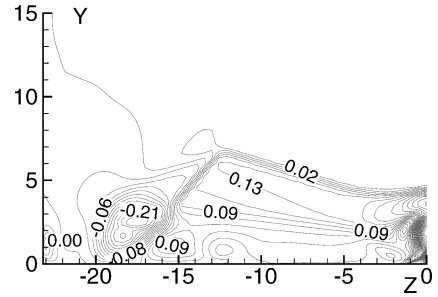

a) No-MGD

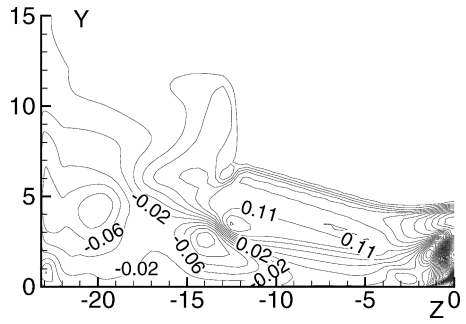

b) Case H5Q1

Fig. 11 Contours of vertical component of velocity on $X = 40.5$ plane.

without MGD (Fig. 10d), has a deleterious impact compared with the no-MGD case. R_3 and S_3 are now not only far more clearly defined, but also new structures are evident near the centerline. For surface streamlines, MGD flow control shows primarily a local effect, whereas the impact of heat release is observed even outside of the immediate region of application.

Figure 11 shows contours of the vertical component of velocity, for no-MGD and H5Q1. Both cases reflect prominent regions of attachment near the corner and near the centerline, where large negative values are observed, whereas off-centerline separation represented by S_3'' is evident in the positive values near $Z \sim -1$. The most significant impact of MGD, as anticipated, is in the region above the plate where control is applied. Here, near the location of the original SS, $Z \sim -13$, the effect reduces the angle from positive (separated) to small negative (attached) values, consistent with the elimination of the line of coalescence in the surface oil pattern. Fundamental differences in the λ shock structure are also apparent.

Effects of control on flow features are more readily explored with pressure and velocity magnitude contours as depicted in Figs. 12 and 13 for H5Q1 and H2Q1, respectively. The reference no-MGD calculation was presented in Figs. 5b and 5c. MGD effects have significant impact for the higher ionization region case, H5Q1. The downstream leg of the λ, closer to the fin surface, essentially disappears, the effect being similar to that observed with bleed.[37] In the region above the line of attachment, both pressure and velocity are more uniform. The smaller ionization region case, H2Q1, shows basically the same qualitative structure as the no-MGD flow shown in Fig. 5, though quantitative differences are evident. The explanation for this drastic difference in response between the two MGD cases is related to the large velocity differences and gradients observed in the λ pattern. H5Q1 reaches essentially into the inviscid high-speed region, thus providing a greater imbalance of motional emf and more striking effects.

Crossflow surface-pressure profiles are presented in Fig. 14a for several computations. H5Q1 shows a substantial reduction in pressure near the fin-plate corner, with maximum values reduced by about 40%. The redistribution of pressure also eliminates the pressure rise associated with SS at $Z \sim -13$ though, as noted earlier, the fluid has a larger streamwise component with MGD control than without. In contrast, H2Q1 yields a diminished pressure rise. Figure 14b exhibits the effect on heat-transfer rates. Because the quantitative values are known to be significantly overpredicted,[18]

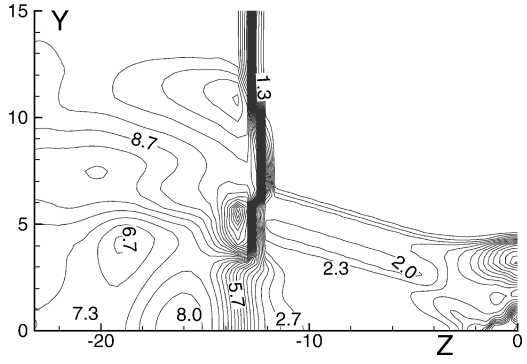

a) Pressure

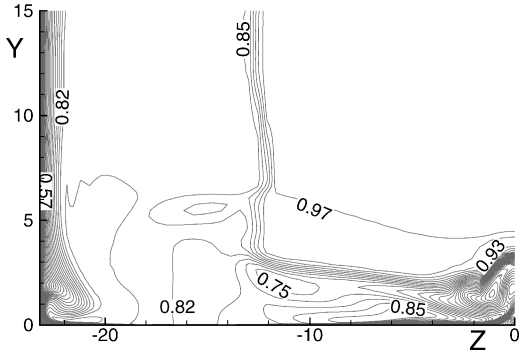

b) *U* magnitude

Fig. 12 Crossflow plane contours, case H5Q1.

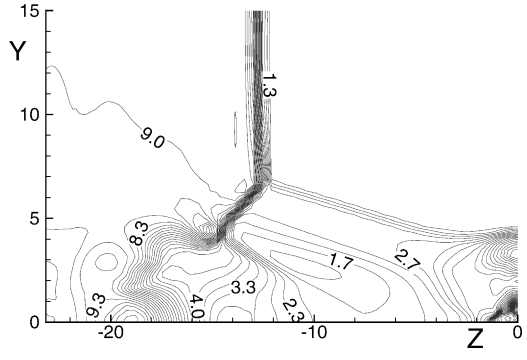

a) Pressure

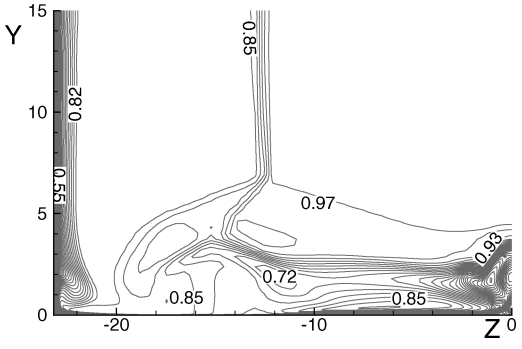

b) *U* magnitude

Fig. 13 Crossflow plane contours, case H2Q1.

only trends are explored by normalizing values with the no-MGD heat-transfer rate. Despite the electrode-less nature of the MGD configuration, an increase is detected in the double-fin case, stemming from the effects of Joule heating. Both H5Q1 and H2Q1 show about 15% increase in the region of control application with minimal effects elsewhere. The heat-addition method yields much higher rates, with peaks approaching about 35% higher than the no-MGD case.

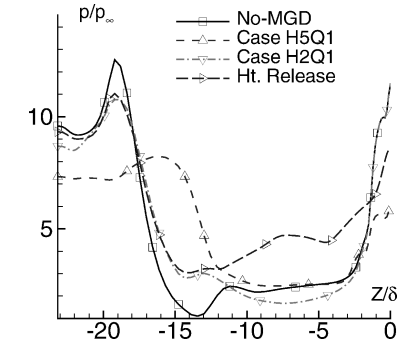

a) Surface pressure

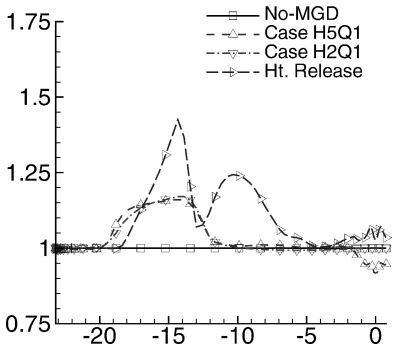

b) Heat transfer (normalized with no-MGD value)

Fig. 14 Effect of control methods on surface pressure and heating at $X = 40.5$.

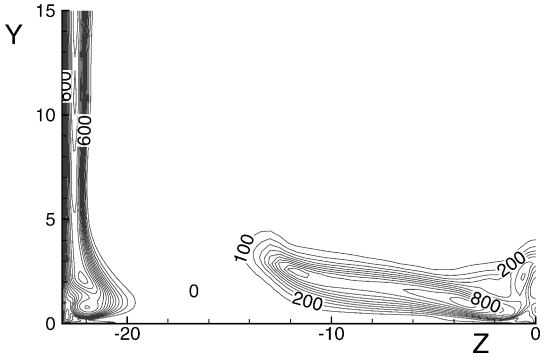

Fig. 15 Eddy viscosity μ_t/μ on crossflow plane, $X = 40.5$, case Q1H1.

Prior to proceeding to a more detailed evaluation of the electromagnetic field vectors, it is noted that the eddy-viscosity model reproduces the anticipated damping effect of the magnetic field on turbulence. Figure 15 exhibits eddy viscosity for case H5Q1 at the crossflow plane, $X = 40.5$. Comparison with Fig. 7 shows that eddy-viscosity values in the ionized region are reduced from the order of 1000 for the no-MGD case to essentially negligible levels. Clearly, the elimination of SS is not associated with heightened turbulence, but rather with ponderomotive force effects, whose structure is explored further below. Scrutiny of Fig. 15 also reveals that convection and diffusion processes yield reduced values of eddy viscosity outside of the region of ionization such as near the centerline.

The electromagnetic fields established are highly three-dimensional and bear very complex spatial relationships to each other. Figure 16a exhibits current magnitude contours at several planes in a perspective view, whereas Fig. 16b plots contours on the $X = 40.5$ cross-flow plane. The current, which has been nondimensionalized by $\sigma_{\text{ref}} U_{\text{ref}} B_{\text{ref}}$, is large principally in two regions, both positioned above the location of the original SS. The first region is near the surface, whereas the second, more elongated in the spanwise direction, is almost directly above it. To highlight energetic interactions, Figure 17 exhibits $\boldsymbol{j} \cdot \boldsymbol{E}$ on the $X = 40.5$ plane. Values

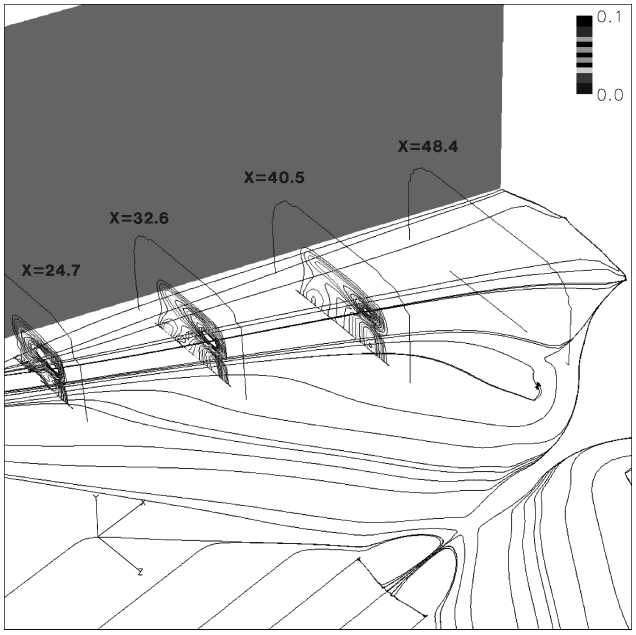

a) Perspective view

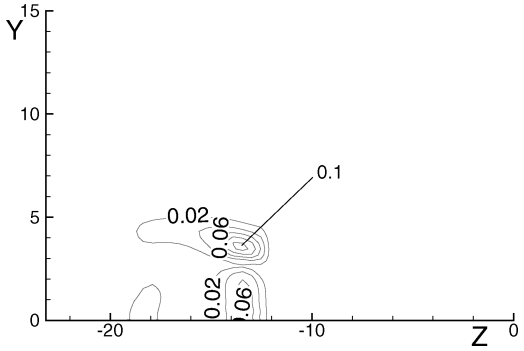

b) Current in cross-flow plane

Fig. 16 Aspects of current distribution.

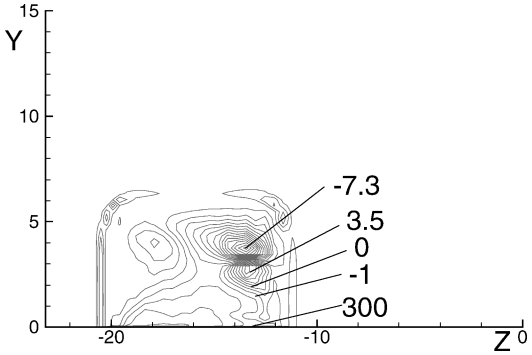

Fig. 17 Input term to energy equation, $\boldsymbol{j} \cdot \boldsymbol{E}$, at $X = 40.5$.

at several locations are marked. The outer region exhibits negative values representing local energy extraction (generator-like). The inner region however displays both negative and positive values. Extremely large positive values, representing acceleration of the flow, are localized in the very near-wall region (accelerator-like). Comparison with H2Q1 (not shown) indicates that the sizes of these generator-like and accelerator-like regions depend upon the extent of the ionized region. Note that not all of the deposited energy is converted into kinetic energy because some is converted into Joule heating, which can be easily surmised from the current pattern of Fig. 16 and recognizing that heating varies quadratically with electric current magnitude and inversely with conductivity.

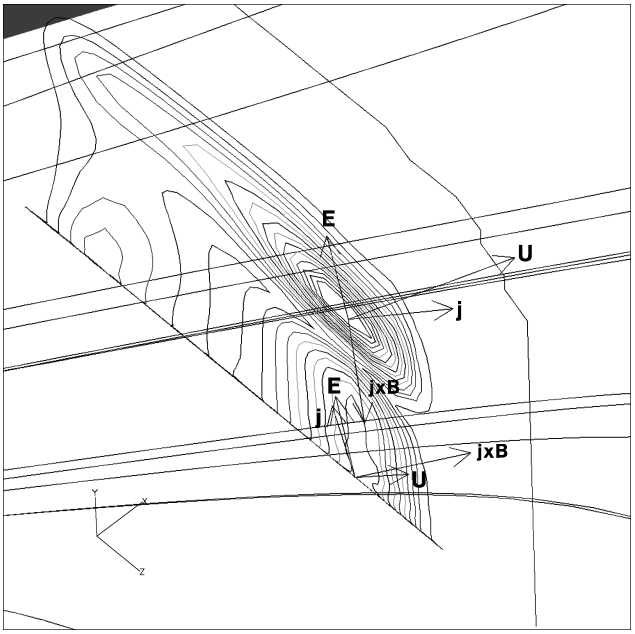

Fig. 18 Spatial relationship between velocity and electromagnetic vectors at peak current locations in $X = 40.5$ plane, case H5Q1.

A succinct view of the complex relationship between the various vectors is provided in Fig. 18, which presents an enlarged view of the electric current contours together with vectors of the velocity, current, electric field, and the body force at the local maximum values of the two regions. Artificial scales have been applied to each vector to highlight the interrelationship. The velocity vector at both locations has a predominantly streamwise and spanwise orientation, being larger in the outer high-speed fluid. However, the induced electric field is relatively similar at both locations. The higher $\boldsymbol{U}$ at the outer location provides a greater $\boldsymbol{U} \times \boldsymbol{B}$ emf, and the current vector forms an obtuse angle with the electric field ($\boldsymbol{E} \cdot \boldsymbol{j} < 0$). This forms the basis of generator-like operation of the local interaction. However, near the surface the $\boldsymbol{U} \times \boldsymbol{B}$ component is smaller than $\boldsymbol{E}$, and the current vector is largely aligned with $\boldsymbol{E}$. Thus, $\boldsymbol{E} \cdot \boldsymbol{j} > 0$, and local operation is accelerator-like. Consequently, Lorentz forces plotted decelerate the flow $\boldsymbol{U} \cdot (\boldsymbol{j} \times \boldsymbol{B}) < 0$ in the high-speed region and accelerate it near the wall $\boldsymbol{U} \cdot (\boldsymbol{j} \times \boldsymbol{B}) < 0$, effectively accomplishing ECBMT.

V. Conclusions

The possibility of utilizing magnetogasdynamic techniques to alleviate or eliminate separation in three-dimensional shock-wave/turbulent boundary-layer interactions is examined, with focus on the phenomenon of secondary separation. Consistent with parameters anticipated in the aerospace environment, the low magnetic Reynolds-number model is employed in conjunction with a simple specified plasma environment. Turbulent effects are reproduced with a two-equation k–ϵ model, modified to account for the damping effect of the magnetic field. The principal mechanism for eliminating separation is based on generating eddy (or closed-loop) currents in the fluid through a suitable ionized region together with insulated walls. The imbalance in motional emf between the low- and high-speed regions yields an induced electric field, which acts to accelerate the near-wall fluid at the expense of far-field fluid momentum. Several parameters, including different conductivity variations and interaction parameters, are explored. The calculations indicate that even though the magnetic field damps values of eddy viscosity in the region of plasma interaction fluid in close proximity to the wall is accelerated locally by ponderomotive forces, and the adverse pressure gradient associated with secondary separation is muted, thus resulting in suppression of separation. The complex three-dimensional interaction between the velocity, current, and induced electric field is elucidated. To separate force and heat-release effects, separate simulations conducted with only heat release in the same region as Joule heating show aggravated effects on secondary separation. Thus, although irreversible electromagnetic heating effects yield increased surface heating, ponderomotive forces dominate in the overall impact on the kinematics of the flowfield structure. Further effort should focus on several major issues, including a determination of the optimum plasma environment, ionization induced heating effects and Hall-current related phenomena.

Acknowledgments

The authors are grateful for Air Force Office of Scientific Research sponsorship under tasks monitored by F. Fahroo, W. Hilbun, and J. Schmisseur. This work was also supported in part by a grant of high-performance computing (HPC) time from the U.S. Department of Defense HPC Shared Resource Centers at the Aeronautical Systems Center, Engineering Research and Development Center, and Naval Oceanographic Office. The authors also acknowledge highly helpful comments and suggestions from several researchers, including S. Macheret, J. Poggie, J. Schmisseur, J. Shang, and M. Visbal.

References

[1]Macheret, S., Shneider, M., and Miles, R., "Magnetohydrodynamic Control of Hypersonic Flows and Scramjet Inlets Using Electron Beam Ionization," *AIAA Journal*, Vol. 40, No. 1, 2002, pp. 74–81.

[2]Park, C., Bogdanoff, D., and Mehta, U., "Theoretical Performance of a Nonequilibrium MHD-Bypass Scramjet," AIAA Paper 2001-0792, Jan. 2001.

[3]Kuranov, A. L., and Sheikin, E. G., "Magnetohydrodynamic Control on Hypersonic Aircraft Under 'Ajax' Concept," *Journal of Spacecraft and Rockets*, Vo. 40, No. 2, 2003, pp. 174–182.

[4]MacCormack, R., "A Conservation Form Method for Magneto-Fluid Dynamics," AIAA Paper 2001-0195, Jan. 2001.

[5]Dietiker, J.-F., and Hoffmann, K., "Modified One-Equation Turbulence Models for Turbulent Magnetohydrodynamic Flows," *Journal of Thermophysics and Heat Transfer*, Vol. 17, No. 4, 2003, pp. 509–520.

[6]Knight, D., "A Selected Survey of Magnetogasdynamic Local Flow Control at High Speeds," AIAA Paper 2004-1191, Jan. 2004.

[7]Gaitonde, D., "Three-Dimensional Flow-Through Scramjet Simulation with MGD Energy-Bypass," AIAA Paper 2003-0172, Jan. 2003.

[8]Gaitonde, D., and Poggie, J., "Elements of a Numerical Procedure for 3-D MGD Flow Control Analysis," AIAA Paper 2002-0198, Jan. 2002.

[9]Gaitonde, D. V., "Higher-Order Solution Procedure for Three-Dimensional Nonideal Magnetogasdynamics," *AIAA Journal*, Vol. 39, No. 11, 2001, pp. 2111–2120.

[10]Gaitonde, D., and Poggie, J., "Simulation of Magnetogasdynamic Flow Control Techniques," AIAA Paper 2000-2326, 2000.

[11]Poggie, J., and Gaitonde, D., "Magnetic Control of Flow past a Blunt Body: Numerical Validation and Exploration," *Physics of Fluids*, Vol. 14, No. 5, 2002, pp. 1720–1731.

[12]Bobashev, S., Mende, N., Sakharov, V., and van Wie, D., "MHD Control of the Separation Phenomenon in a Supersonic Xenon Plasma Flow. I," AIAA Paper 2003-168, Jan. 2003.

[13]Kuranov, A., and Sheikin, E., "The Potential of MHD Control for Improving Scramjet Performance," AIAA Paper 99-3535, June 1999.

[14]Gaitonde, D., and Poggie, J., "Implicit Technique for Three-Dimensional Turbulent Magnetoaerodynamics," *AIAA Journal*, Vol. 41, No. 11, 2003, pp. 2179–2293.

[15]Gaitonde, D., and Miller, J., "Numerical Exploration of Shock Interaction Control with Plasma-Based Techniques," AIAA Paper 2003-3483, June 2003.

[16]Zheltovodov, A., and Maksimov, A., "Hypersonic Crossing-Shock-Waves/Turbulent Boundary Layer Interactions," Russian Academy of Sciences, Tech. Rept. Final Rept., EOARD Contract F61775-98-WE091, Novosibirsk, Russia, July 1999.

[17]Schuelein, E., and Zheltovodov, A., "Development of Experimental Methods for the Hypersonic Flows Studies in Ludwieg Tube," *Proceedings of the International Conference on the Methods of Aerophysical Research: Part 1*, Vol. 2, Inst. of Theoretical and Applied Mechanics, Novosibirsk, Russia, 1998, pp. 191–199.

[18]Knight, D., and Degrez, G., "Shock Wave Boundary Layer Interactions in High Mach Number Flows—A Critical Survey of Current CFD Prediction Capabilities," AGARD, Tech. Rept., AR-319, Vol. 2, Dec. 1997.

[19]Gaitonde, D., Shang, J., Garrison, T., Zheltovodov, A., and Maksimov, A., "Three-Dimensional Turbulent Interactions Caused by Asymmetric Crossing-Shock Configurations," *AIAA Journal*, Vol. 37, No. 12, 1999, pp. 1602–1608.

[20]Schmisseur, J., and Gaitonde, D., "Numerical Investigation of Strong Crossing Shock-Wave/Turbulent Boundary-Layer Interactions," *AIAA Journal*, Vol. 39, No. 9, 2001, pp. 1742–1749.

[21]Schmisseur, J., and Gaitonde, D., "Numerical Investigation of New Topologies in Strong Crossing Shock-Wave/Turbulent Boundary-Layer Interactions," AIAA Paper 2000-0931, Jan. 2000.

[22]Mitchner, M., and Kruger, C., *Partially Ionized Gases*, Wiley, New York, 1973.

[23]Rosa, R., *Magnetohydrodynamic Energy Conversion*, McGraw–Hill, New York, 1968.

[24]Gaitonde, D. V., and Poggie, J., "Implicit Technique for Three-Dimensional Turbulent Magnetoaerodynamics," *AIAA Journal*, Vol. 41, No. 11, 2003, pp. 2179–2191; also AIAA Paper 2001-2736, June 2001.

[25]Kenjeres, S., and Hanjalic, K., "On the Implementation of Effects of Lorentz Force in Turbulence Closure Model," *International Journal of Heat and Fluid Flow*, Vol. 21, No. 3, 2000, pp. 329–337.

[26]Roe, P., "Approximate Riemann Solvers, Parameter Vectors and Difference Schemes," *Journal of Computational Physics*, Vol. 43, No. 2, 1981, pp. 357–372.

[27]van Leer, B., "Flux-Vector Splitting For the Euler Equations," ICASE, Tech. Rept. 82-30, Langley, VA, Sept. 1982.

[28]van Leer, B., "Towards the Ultimate Conservation Difference Scheme V, A Second-Order Sequel to Godunov's Method," *Journal of Computational Physics*, Vol. 32, No. 2, 1979, pp. 101–136.

[29]Bush, W. B., "The Stagnation-Point Boundary Layer in the Presence of an Applied Magnetic Field," *Journal of the Aerospace Sciences*, Vol. 28, No. 8, 1961, pp. 610, 611, 630.

[30]Bush, W. B., "Compressible Flat-Plate Boundary-Layer Flow with an Applied Magnetic Field," *Journal of the Aero/Space Sciences*, Vol. 27, No. 1, 1960, pp. 49–58.

[31]Zheltovodov, A., "Shock Waves/Turbulent Boundary-Layer Interactions—Fundamental Studies and Applications," AIAA Paper 96-1977, June 1996.

[32]Panaras, A., "Algebraic Turbulence Modelling for Swept Shock-Wave/Turbulent Boundary-Layer Interactions," *AIAA Journal*, Vol. 35, No. 3, 1997, p. 456.

[33]Thivet, F., Knight, D., Zheltovodov, A., and Maksimov, A., "Some Insights in Turbulence Modeling for Crossing-Shock-Wave/Boundary-Layer Interactions," AIAA Paper 2000-0131, Jan. 2000.

[34]Settles, G., and Dolling, D., "Swept Shock Wave/Boundary-Layer Interactions," *Tactical Missile Aerodynamics: General Topics*, Vol. 1, AIAA, Reston, VA, 1997, pp. 297–379.

[35]Alvi, F., and Settles, G., "Physical Model of the Swept Shock Wave/Boundary-Layer Interaction Flowfield," *AIAA Journal*, Vol. 30, No. 9, 1992, pp. 2252–2258.

[36]Gaitonde, D., and Shang, J. S., "Structure of a Turbulent Double-Fin Interaction at Mach 4," *AIAA Journal*, Vol. 33, No. 12, 1995, pp. 2250–2258.

[37]Gaitonde, D., and Knight, D., "A Numerical Investigation of Effect of Bleed on 3-D Turbulent Interactions Due to Sharp Fins," *AIAA Journal*, Vol. 29, No. 11, 1991, pp. 1878–1885.

K. Fujii
Associate Editor